ENGINEERING

Breaking the absorption limit of Si toward SWIR wavelength range via strain engineering

Ajit K. Katiyar[1], Kean You Thai[1], Won Seok Yun[2], JaeDong Lee[2], Jong-Hyun Ahn[1]*

Copyright © 2020 The Authors, some rights reserved; exclusive licensee American Association for the Advancement of Science. No claim to original U.S. Government Works. Distributed under a Creative Commons Attribution NonCommercial License 4.0 (CC BY-NC).

Silicon has been widely used in the microelectronics industry. However, its photonic applications are restricted to visible and partial near-infrared spectral range owing to its fundamental optical bandgap (1.12 eV). With recent advances in strain engineering, material properties, including optical bandgap, can be tailored considerably. This paper reports the strain-induced shrinkage in the Si bandgap, providing photosensing well beyond its fundamental absorption limit in Si nanomembrane (NM) photodetectors (PDs). The Si-NM PD pixels were mechanically stretched (biaxially) by a maximum strain of ~3.5% through pneumatic pressure–induced bulging, enhancing photoresponsivity and extending the Si absorption limit up to 1550 nm, which is the essential wavelength range of the lidar sensors for obstacle detection in self-driving vehicles. The development of deformable three-dimensional optoelectronics via gas pressure–induced bulging also facilitated the realization of unique device designs with concave and convex hemispherical architectures, which mimics the electronic prototypes of biological eyes.

INTRODUCTION

Developing low-cost flexible/bendable optoelectronic devices such as bioinspired imaging systems (*1*, *2*), photodetectors (PDs) (*3*), and photovoltaic cells (*4*) with a capability to operate under near-infrared (NIR) wavelength at room temperature is of immense interest for security, light tracking, telecommunications, and energy applications. In particular, the development of PDs that can detect the spectral range of short-wavelength infrared (SWIR) (1300 to 2000 nm) is in high demand for the lidar sensors used in self-driving vehicles. The lidar device installed on an autonomous vehicle provides a 360° view of the surrounding objects and works as an eye of the driverless vehicle. The use of SWIR light is essential for the lidar system used in self-driving vehicles because high-power light of ultraviolet-NIR wavelength (250 to 1000 nm) can cause irreparable harm to the retina of the human eye. InGaAs-based sensors, which have been currently used to detect this range of wavelength, have the disadvantages of expensive production cost and incompatibility with complementary metal-oxide semiconductor (CMOS) platform.

Silicon has already been used as the basic building block in several photonic applications for the visible wavelength range over the past few decades. However, the IR photosensing of Si-based devices is limited owing to the fundamental optical bandgap of 1.12 eV (~1110 nm). A few attempts have been made in the past to extend the photoresponse of bulk silicon toward the SWIR range by alloying it with Ge (*5*, *6*). The addition of Ge into Si ($Si_{1-x}Ge_x$, $0 \leq x \leq 1$) increases the absorption cutoff toward the higher wavelength. Depending on the Ge content (x) in the alloy, the bandgap can be tuned between 1.12 eV ($x = 0$) and 0.66 eV ($x = 1$), which can further extend via the application of strain into the alloyed system. Although SiGe alloy systems have been extensively studied, the practical implementations of such systems are limited due to several constraints such as restricted growth of thick $Si_{1-x}Ge_x$ layers (<15 nm) and indirect nature of $Si_{1-x}Ge_x$ alloy (for $x < 0.75$), which leads researches to look for alternative approaches to obtain the NIR optical activity in pristine Si. Other alternatives such as creating sub-bandgap energy levels by intentionally damaging the silicon lattice via hyper-doping with chalcogen or other metal atoms (*7*–*10*) have also been used. These approaches involved several processing complexities with serious compromise in the inherent CMOS compatibility of Si. Thus, to maintain the CMOS compatibility, direct modification of the electronic band structure of pristine Si to absorb SWIR photons would be of substantial interest.

It has been theoretically claimed that the band structure of Si can be substantially modified under the influence of compressive or tensile strain (*11*, *12*). Specifically, under the influence of tensile strain, the increase in lattice spacing and change in crystal symmetry provide a pronounced shift in the energy band edges of Si, thereby leading to a decrease in the bandgap and an increase in the effective masses of charge carriers (*13*, *14*). The reduction in optical bandgap can provide an opportunity to capture photons with energies less than the fundamental bandgap of Si (*15*), and the increase in the effective masses can lead to an increase in carrier mobility (*14*, *16*). Many theoretical and experimental studies have been conducted to investigate the effect of strain on the band structure of bulk and other low-dimensional systems of Si such as nanowires (*16*), nanocrystals (*17*), and nanomembranes (NMs) (*15*). An experimental study conducted on a two-dimensional (2D) silicon on insulator (SOI) reported that a uniaxial strain of 1.8% can induce shrinkage in the indirect bandgap of ~0.3 eV (*18*). It has also been reported that the effect of biaxial strain on bandgap reduction is more prominent than that of uniaxial strain (*19*, *20*). Thus, the application of biaxial tensile strain into the Si lattice can notably modify the optoelectronic properties and tune the photoresponse toward the SWIR wavelength region.

Strain engineering for optoelectronic devices was initially proposed for the enhancement of efficiency in InGaAsP-based lasers (*21*, *22*); thereafter, it was successfully implemented in Si/Ge-based waveguides and other photonic devices (*23*–*25*). The most commonly adopted strain-engineering approaches for large-area Si rely on the deposition of a SiN stressor or heteroepitaxial growth of Si on top of the lattice-mismatched substrates (*23*, *25*). However, the applied strain through the aforementioned approaches is limited to less than 1%. Moreover, these approaches have disadvantages that include high processing costs and interfacial defects. Alternatively, to obtain a higher level of strain, other approaches such as patterning of suspended Si bridges on strained SOI (*15*, *26*) and the microelectromechanical

[1]School of Electrical and Electronic Engineering, Yonsei University, Seoul 03722, Republic of Korea. [2]Department of Emerging Materials Science, DGIST, Daegu 42988, Republic of Korea.
*Corresponding author. Email: ahnj@yonsei.ac.kr

Downloaded from http://advances.sciencemag.org/ on December 4, 2020

system–based tensile loading in 1D nanowires have also been demonstrated (*27*, *28*). Unfortunately, these techniques can only provide uniaxial strain and are limited to fundamental studies on mechanical and electrical properties; they are not very suitable for stretchable/bendable optoelectronic device applications with broad-range wavelength tunability. Therefore, the implementation of a higher level of biaxial strain in Si NMs via a practical approach shall be of enormous interest for extending the fundamental optical absorption onset of Si toward the SWIR wavelength.

Here, we report the notable photoresponse from Si well beyond its optical bandgap limit by applying biaxial tensile strain into the Si lattice. The shrinkage in bandgap due to the biaxial tensile strain made it possible to overcome the absorption limit of Si. To demonstrate the room temperature SWIR imaging capability, we fabricated metal-semiconductor-metal (MSM)–type PD arrays on ultrathin Si NMs (<10 nm) on a thin polymer substrate. The biaxial tensile strain on each pixel of the 6 × 6 array MSM devices was exerted in a highly controlled manner by mounting the array devices on a bulge test setup. In this study, by combining the mechanical excellence of ultrathin Si and strain engineering in the pneumatic bulging–induced formation of deformable optoelectronics with hemispherical geometry, broadband visible-to-SWIR imaging capability was achieved, which appears to be very promising for realizing emerging technologies such as the lidar sensors for self-driving vehicles and bioinspired imaging systems.

RESULTS

The target photodiode array matrix is patterned through a photolithography process and then transferred onto the polyimide (PI) film (Fig. 1, A and B, and fig. S1) (see Materials and Methods). Under a controlled flow of N_2, the pressure inside the sample holder cavity increased, which enabled the bulging in the PI membrane (fig. S2). Figure 1C shows the scanning electron microscopy (SEM) images of the bulged PI film under convex and concave geometry containing the fabricated array devices.

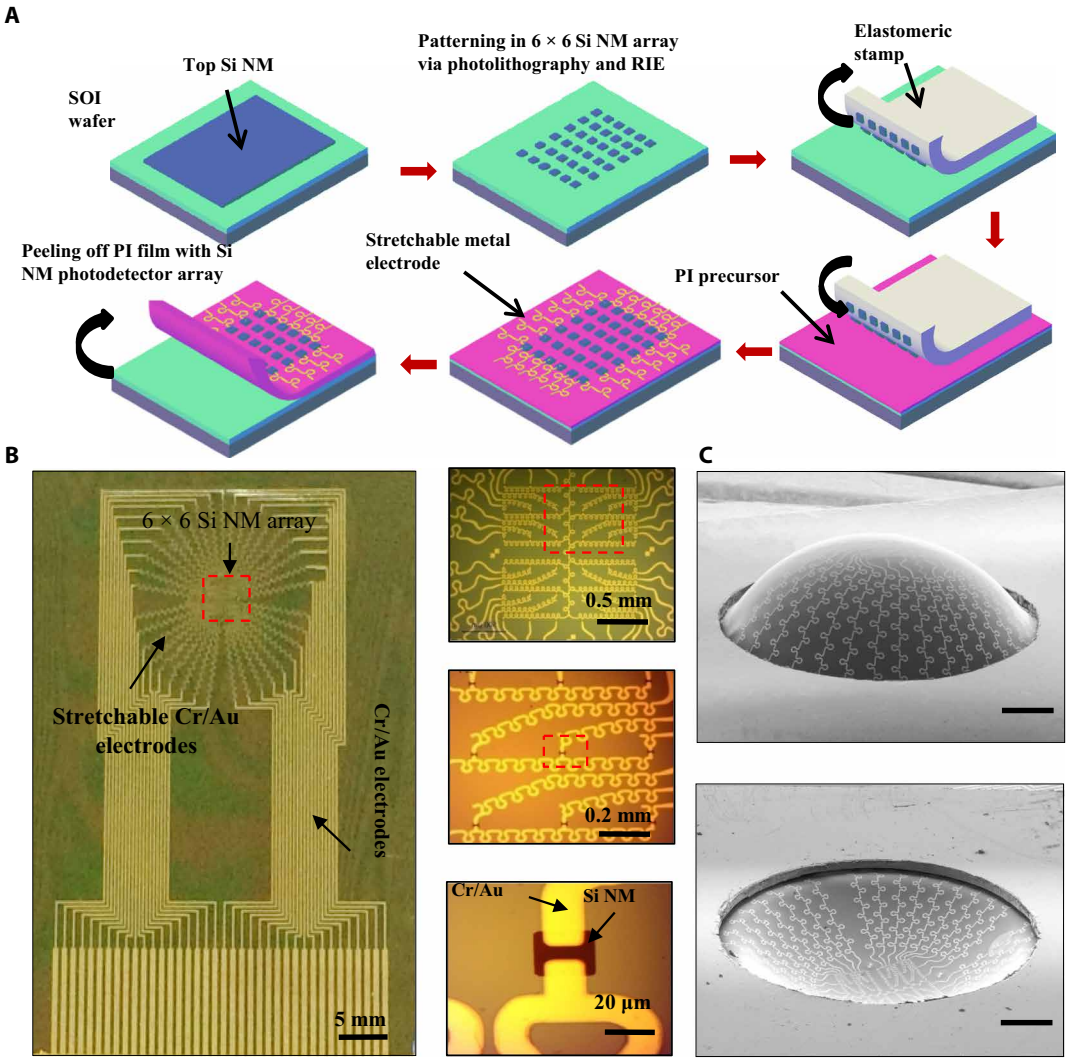

Fig. 1. Fabrication of 6 × 6 Si NM array devices for strain-controlled stretchable PD. (**A**) Schematic illustration of device fabrication. RIE, reactive ion etching. (**B**) Photograph of a fabricated device on PI-coated SiO_2/Si substrate and corresponding magnified view of device sections. (**C**) SEM images of convex (top) and concave (bottom) hemispherical shape of bulged PI film containing a 6 × 6 Si-NM PD array. Scale bars, 0.5 mm.

Downloaded from http://advances.sciencemag.org/ on December 4, 2020

The maximum strain value in the Si NM samples of different thickness was measured via Raman spectroscopy. Figure 2A shows the obtained Raman spectra of the 10-nm-thick Si NM sample recorded with increasing gas pressure. The spectra consist of two peaks, one Si-Si vibrational mode peak near 520 cm^{-1} and the other at approximately 570 cm^{-1} originated from the underneath PI film. With gradual increase in pressure inside the sample holder cavity up to 2000 torr, a systematic shift toward a lower wave number side along with the increase in intensity was observed in the Si-Si vibrational mode, whereas the peak position and intensity of the PI remained unchanged. The real-time biaxial strain value ($\varepsilon_{biaxial}$) in the plane of a Si NM subjected to increasing pressure was directly estimated by observing the shift in Raman peak near 520 cm^{-1} using the following relationship: $\varepsilon_{biaxial}$ (%) = $-0.144 \times (\omega_{bulk} - \omega_{strained})$, where 0.144 is the strain-shift coefficient for biaxial strain, and ω_{bulk} and $\omega_{strained}$ represent the peak positions of the Si-Si vibration mode for bulk and strained Si NMs, respectively; the negative sign in the right-hand side represents tensile strain (*29*). The values of maximum applied strain into Si NM samples of different thicknesses are summarized in Fig. 2B. The obtained graph indicates that the maximum applied biaxial strain value gradually increases as the Si NM thickness decreases. A 10-nm-thick sample (without metal electrodes) exhibited a maximum strain of 4.36%. With a reduction in the NM thickness further below 10 nm, the maximum applied strain decreases to a relatively low value of 4.1% for a 4-nm-thick Si NM. It can be noticed that the cracks in the Si NMs with thickness exceeding 10 nm were aligned at an angle of 90° (inset of Fig. 2B), whereas for the samples with thickness below 10 nm, the cracks were oriented randomly

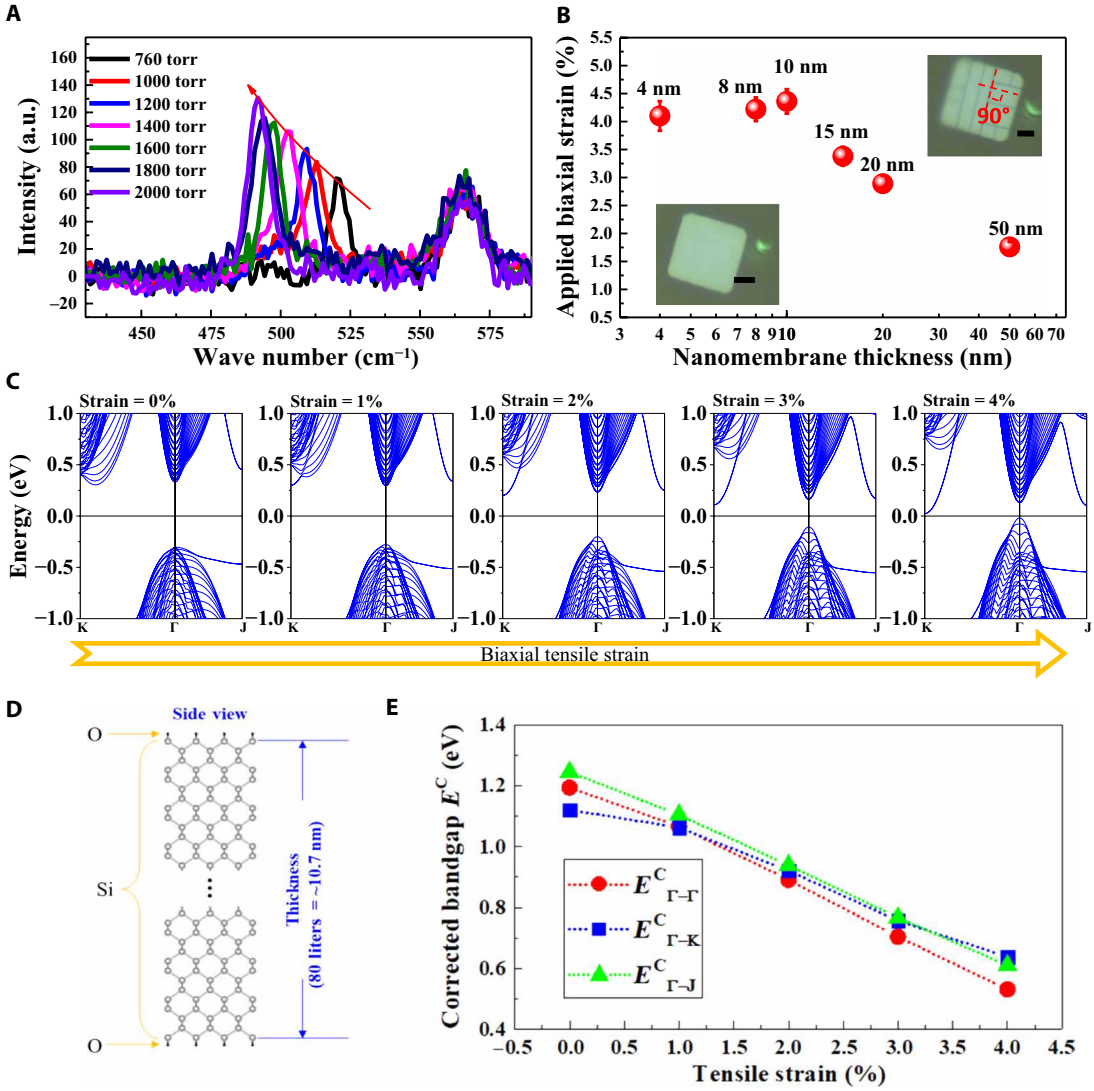

Fig. 2. Strain and photodetection characteristics of single MSM device fabricated on 20 μm by 20 μm–sized 10-nm-thick Si NM and theoretical calculation of electronic band structure. (**A**) Raman spectra of 10-nm-thick Si NM sample recorded with increasing pressure. The spectra show the Raman scattering intensity enhancement and peak position shift toward the lower wave number side with increasing pressure. a.u., arbitrary units. (**B**) Maximum applied biaxial strain value in Si NMs of different thicknesses via the bulging process just before fracture. The inset shows the Si NM before (bottom left) and after fracture (top right). (**C**) Strain-dependent electronic band structure of 10-nm-thick Si NM with an applied biaxial strain of up to 4%. (**D**) Schematic representation of atomic arrangements of ~10-nm-thick Si NM used in theoretical calculation. (**E**) Bandgap values of different transitions extracted from the calculated energy band diagram for 10-nm-thick Si NM sample subjected to increasing biaxial tensile strain.

Downloaded from http://advances.sciencemag.org/ on December 4, 2020

(fig. S3, A and B). Random fractures at a relatively low applied pressure result in the saturation and reduction of the maximum applied strain value (*30*, *31*).

To validate the role of bandgap reduction in SWIR light detection, we theoretically calculated the electronic energy band diagrams of 10-nm-thick Si NM samples at different applied biaxial strain values in the range of 0 to 4%, and the results are presented in Fig. 2C. Computational details and model are described in Fig. 2D and fig. S4 (*32*, *33*). The calculation results presented in the energy band plots exhibit a reduction in bandgap at gap at Γ-point with increase in biaxial strain value. The bandgap values for Γ-Γ, Γ-K, and Γ-J transitions extracted at different strain levels are summarized in Fig. 2D, which are corrected by adding Δ because the electronic structure calculation with the generalized gradient approximation (GGA) is well known to underestimate the bandgap (*34*). Most of the structural effects due to strain would be captured by the GGA calculation so that Δ would be less sensitive to the strain. From a comparison of the unstrained Si NM with the bulk Si, Δ = 0.49 eV is taken. It must be noted that the applied strain of 1.8% provided a reduction of ~0.20 eV in the Γ-Γ bandgap (bandgap = 0.92 eV), which corresponds to a wavelength of 1347 nm. Similarly, a biaxial strain of 3.0% provided a reduction of 0.36 eV (bandgap = 0.76 eV), which corresponds to a wavelength of 1630 nm.

Before examining the large-area 6 × 6 matrix imaging system, we evaluated the strain-induced photosensing tunability in a single MSM-PD pixel fabricated with 10-nm-thick Si NM. The PDs with MSM configuration have slow and relatively modest photoresponse in comparison to the devices with p-n or p-i-n geometry. To compare the optoelectronic performance of MSM and p-n junction pixels fabricated with low-dimensional Si (≤10 nm thickness), we also prepared p-n diode devices on 100- and 10-nm-thick Si NM via selective ion implantation. Both MSM and p-n junction devices fabricated with 10-nm-thick Si NM exhibited similar current-voltage characteristics under dark and light exposure (figs. S5 and S6) (*35*).

Figure S7 shows a digital photograph of the Si-NM PD array mounted on the bulge test setup during the photoresponse measurement under the exposure of a 532-nm laser. Under dynamically increasing straining pressure in the bulge test cavity from 770 torr (atmospheric pressure) up to a level of 1600 torr, a systematic bulging was realized (Fig. 3A). Figure 3B shows the transient photoresponse recorded at an applied bias of 2 V under pulsed illumination of different lights, including 405-, 532-, 650-, 980-, 1310-, and 1550-nm light, for a single device. By maintaining the incident optical power constant for each wavelength, the pressure inside the bulge test cavity was gradually increased; this led to an increase in strain in the Si NMs. The photoresponsivity was calculated for each wavelength under the increasing strain using the relationship $R_{ph} = I_{ph}/P_{in}$, where I_{ph} is the photocurrent and P_{in} is the incident optical power. For the unstrained case, responsivity values of 0.67, 3.37, 11.38, and 44.21 mA/W were observed for incident wavelengths of 405, 532, 650, and 980 nm, respectively, with no response for the 1310- and 1550-nm light. The increasing trend in responsivity with the increase in wavelength up to 980 nm agrees well with the optical absorption characteristics of the crystalline Si (*36*). It may be noted that the observed responsivity values in the fabricated MSM PD on a 10-nm-thick Si NM were relatively small in comparison to those of the commercially available and other reported Si-based PD systems (*37*). A clear increment in photocurrent was recorded under the constant intensity exposure of 532-nm light with increasing strain values (fig. S8B). In a similar way, the increase in responsivity for each wavelength with respect to the applied biaxial strain can be observed (Fig. 3B). For example, at a wavelength of 980 nm, the responsivity increased from 44.21 to 62.37 mA/W from the unstrained condition to a biaxial strain of 3.5%, respectively. To qualitatively quantify the light absorption that governs the optical responsivity in Si NMs of different thickness, we carried out the photocurrent measurement on Si NM PD pixels fabricated on 20-, 10-, and 4-nm-thick Si NMs. The photocurrent recorded for different samples revealed a reduced optical absorption with decrease in NM thickness (figs. S9 and S10). The linear dynamic range (LDR) is another crucial parameter for PDs, which depends on the NM thickness and characterizes the incident light intensity range in which the PDs have a constant photo response. The Si NM PD pixel fabricated with 10-nm-thick Si demonstrates an LDR value of ~67.6 dB for 532-nm light, which is a reasonably good value for the effective operation of a PD (fig. S11) (*38*). Although the responsivity values and the effect of strain on thick Si NM samples are more pronounced, the thick samples have low value of biaxial strain, and as a result, thin thickness is preferred for broad wavelength tunability.

It is speculated that the increase in photoresponsivity was due to the combined effects of the enhancement in optical absorption and photoinduced charge carrier mobilities at elevated strain levels. It is theoretically reported that strain can substantially influence the band edges of optical absorption owing to the change in the symmetry of wave functions and the optical matrix element (*12*, *15*), and mobilities of both the charge carriers increase under the strain-induced modification in effective masses and reduction in phonon scattering (*14*, *16*). With the increase in applied biaxial strain, the fabricated MSM devices exhibited photosensing beyond the fundamental photoabsorption limit of Si (~1100 nm). At a strain level of ~1.8%, clear photodetection can be observed under the modulated exposure of 1310-nm light. With further increase in strain, the photoresponse was increased with much clearer on/off feature at a higher strain level of ~3.5%. Similarly, distinguishable changes in the photocurrent measured in the dark and for the exposure of 1550-nm incident light were also observed for a biaxial strain above 3.2%, which were absent for the unstrained and 1.8% strain levels.

To investigate the effect of strain on near–band edge absorption, we transferred Si NMs onto the textured substrates, which induce strain (figs. S12 to S14) (*30*, *39*, *40*). The 10-nm-thick Si NM samples were transferred on SiO_2/Si substrates containing linear strips and conical shaped textures with sharp top edges that create uniaxial and biaxial strain of ~1.4%, respectively. Although this straining approach provided relatively low strain values in comparison to the bulge testing, it offers the opportunity to fabricate complete MSM devices on a SiO_2/Si substrate, thus facilitating the measurement of photocurrent near the band edge (NBE). The NBE photocurrent spectra measured for different samples revealed a clear extension in the absorption cutoff toward higher wavelength for both the uniaxially and biaxially strained Si NM PD pixels. The extension in absorption cutoff was more prominent for biaxially strained Si due to the effective shrinkage in optical bandgap (fig. S14).

To realize the strain-induced tunability in the photodetection of Si up to SWIR wavelength range, the responsivity versus wavelength data were recorded under increasing strains (fig. S15). At a strain level of 3.5%, the fabricated Si-NM MSM PD exhibited a broad photodetection range starting from a wavelength of 405 nm up to 1550 nm, which is ~450 nm beyond the fundamental bandgap limit of Si (i.e., ~1.1 eV). The observed photoresponse for 1310- and 1550-nm light

Downloaded from http://advances.sciencemag.org/ on December 4, 2020

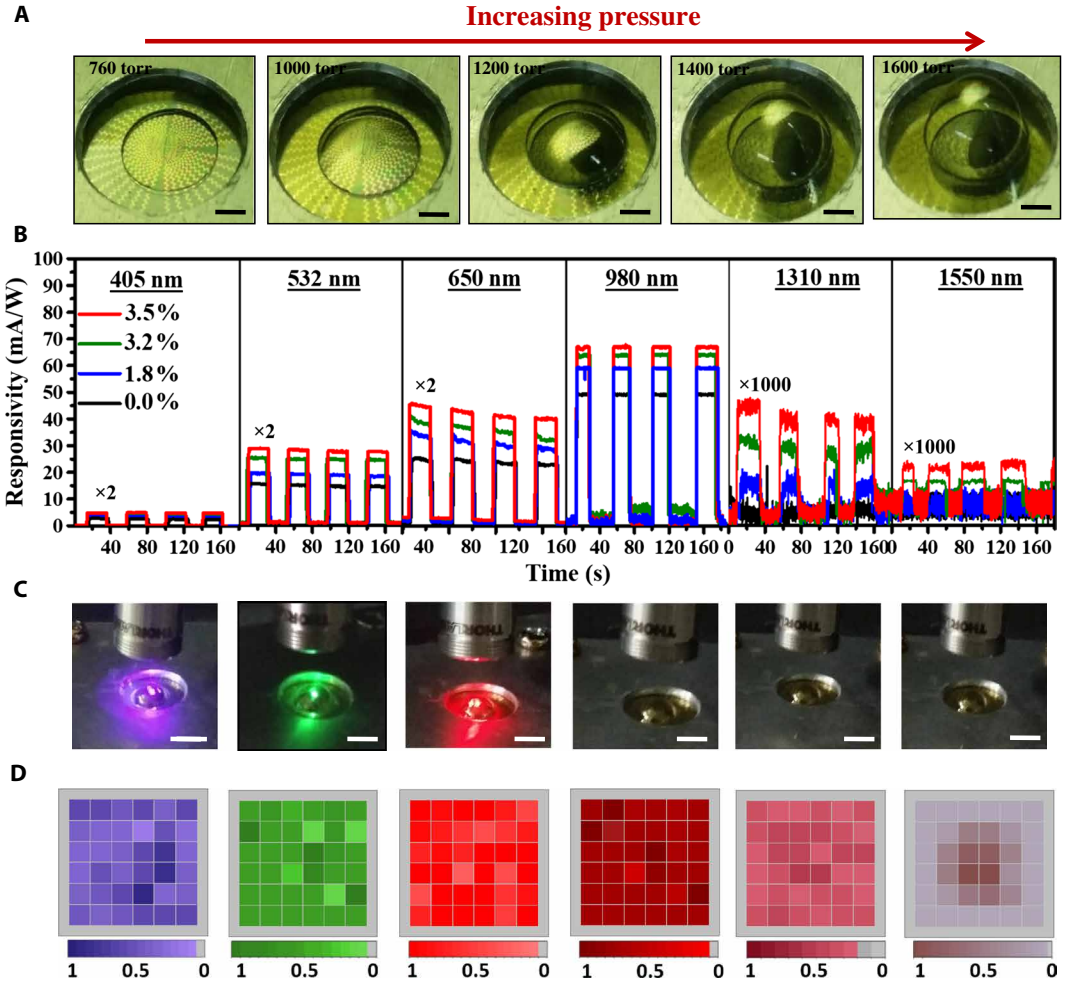

Fig. 3. Strain-induced photoresponse and imaging characteristics of fabricated PD array. (**A**) Photograph of the 6 × 6 Si-NM PD array device mounted on bulge test setup with increasing pressure (scale bars, 1 mm). Photo credit: Ajit K. Katiyar, Yonsei University. (**B**) Strain-dependent transient photoresponse of single 10-nm-thick Si NM device measured under incident light of different wavelengths, from 405 to 1550 nm. The plots reveal the photosensing capability of the 10-nm-thick Si NM device beyond the Si photoabsorption wavelength range (400 to 1100 nm) under the applied strain. A clear on/off in photoresponse can be noticed under the 1550-nm light above the 3.5% applied biaxial strain. (**C**) Digital photographs of the Si-NM PD array device captured during imaging with lights of various wavelengths (scale bars, 3 mm). Photo credit: Ajit K. Katiyar, Yonsei University. (**D**) Corresponding photocurrent mapping images recorded under incident light of different wavelengths.

under biaxial strain of 1.8 and 3.2%, respectively, are congruent with the calculation results shown in Fig. 2D. The measured responsivity values for wavelengths 1310 and 1550 nm are ~35 and 4 μA/W, respectively, at an applied biaxial strain of ~3.5%, which was relatively low in comparison to those measured in the visible wavelength region (~44.21 mA/W under 980-nm illumination). The issue of low photoresponsivity in SWIR range beyond the wavelength of 1100 nm can be addressed by integrating Si NM surface with PbS quantum dots (fig. S16) (*30*, *41*). Most of the Si-based commercial PDs that are typically made with a p-i-n configuration and fabricated on thick Si can provide relatively high responsivity (a few hundred mA/W) up to a wavelength of ~1100 nm. However, these PDs cannot detect light with wavelengths beyond 1100 nm, whereas our strained Si PD has an intriguing advantage over commercial Si PDs; it can detect incident light with wavelengths well beyond 1100 nm. It is known that the application of compressive or tensile strain in the Si crystal alters the lattice spacing, which can modify the band structure (*12*, *13*). Specifically, the application of tensile strain can reduce the bandgap, thereby enabling the extension of the optical absorption into the SWIR wavelength region. Karazhanov *et al.* (*12*) theoretically reported that a negative straining pressure of 12 GPa in bulk Si can reduce the bandgap of Si up to 0.8 eV. In another study, Munguia *et al.* (*18*) experimentally demonstrated a reduction of 239 meV in the Si bandgap at a biaxial strain of 1.54% using a low-temperature photoluminescence measurement. In our straining approach of bulge testing, we were able to apply a substantially high level of biaxial tensile strain (approximately 3.5%), and as a result, the bandgap of the Si NM was reduced to 0.8 eV (i.e., wavelength of 1550 nm) with Δ = 320 meV, which exceeded the optical absorption cutoff in Si NM.

After analyzing the SWIR photosensing features of a representative single Si MSM device, we demonstrated the strain-induced SWIR imaging capability by fabricating a prototype of a 6 × 6 array square matrix system. Figure 3C shows the digital photographs recorded under the exposure of light with different wavelengths. The incident lights of 980, 1310, and 1550 nm are beyond the range of the visible wavelength spectrum, and therefore, they cannot be observed by the

Downloaded from http://advances.sciencemag.org/ on December 4, 2020

eyes or a normal camera. The photocurrent-distribution images obtained under the exposure of different lights are presented in Fig. 3D. We can notice the photosensing and imaging capability of the strained Si-NM PD pixel array under the exposures of 1310- and 1550-nm light along with the other wavelengths of visible lights at a straining pressure of 1600 torr. Most of the 36 fabricated PD (~32 pixels) pixel units exhibited almost similar photosensing features for all wavelengths, although a few of them also showed a slightly different photoresponse. The electrical and photoresponse characteristics of all the fabricated pixels were expected to be the same in the ideal case; however, in the real case, the different contact resistances due to the presence of the unavoidable native oxide on the Si NM surface may have provided slightly different optoelectronic characteristics to some of the MSM pixels. Particularly, for the exposure of 1550-nm light, the photoresponse exhibited by a majority of the inner pixels of the 6 × 6 matrix was higher than that exhibited by the pixels located outward. The strain value at the highest applied pressure of 1600 torr was measured in each Si NM pixel through Raman spectroscopy, and the results are presented in fig. S17. A nonuniform strain distribution was observed across the different pixels of the 6 × 6 matrix. Under a straining pressure of 1600 torr, a biaxial strain of ~2.5% was applied in the outermost pixels, whereas the inner pixels were stretched with the relatively higher strain of ~3.6%. The increasing strain gradient toward the inner pixels of the PD matrix consequently provided higher photocurrent in the inner PD pixels.

In normal gas pressure–driven bulge test experiments, with the increase in applied pressure above a particular level, the bulge progressively enlarges with increase in area, resulting in a hemispherical structure (*42*, *43*). Under the gas pressure–induced biaxial tension, the area at the topmost part of the hemisphere tends to stretch more in comparison with the area near the periphery, which results in an increase in strain in the inner pixels of the PD matrix. To achieve a uniform strain in each PD pixel, we attempted to stretch the PI film containing the Si NM pixels horizontally using a specially designed radial tensioning stage (fig. S18). The in-plane radial stretching in the PI film addresses the issue of strain gradient in the outer to inner pixels of the Si NM matrix. However, manual translation of the metal plates using hands to stretch the bonded PI films provided a relatively nonuniform stretching, which results in a random value of applied strain in the NM pixels in the range of 1.98 to 2.86% (*30*). Thus, this approach is not as suitable for device fabrication as the gas pressure–induced bulging, which additionally has the capability to produce hemispherical 3D shapes. Therefore, we used the bulge test approach for applying strains on the Si NM pixels and performed SWIR light detection. Last, to demonstrate the strain-induced tuning in photosensing, we recorded a photocurrent pattern of the alphabet "Y" fabricated on a glass substrate, similar to a shadow mask (Fig. 4, A and B), from the 6 × 6 matrix PD system subjected to increasing biaxial strains under the exposure of 1310-nm light, and the results are illustrated in Fig. 4C. A noticeable photocurrent was detected in most of the pixels at a strain level of ~1.8%, which resulted in a clear imaging of the Y alphabet under 1310-nm SWIR light. The effect of strain on tuning in the optical absorption onset is evident in the obtained mapping images. Specifically, no signal was detected for the unstrained condition, whereas at a straining pressure exceeding 1200 torr (biaxial strain of ~1.8%), the PD pixels began to respond under exposure to light. As the straining pressure into the bulge test cavity increased further, there was an increase in strain in each PD pixels, and consequently, the photocurrent also increased progressively. A clear realization of imaging a Y can be noticed at a straining pressure of 1600 torr, which corresponds to the maximum strain of ~3.5% (movie S1).

Along with the strain-induced benefits in photosensing applications, the evolution of a hemispherical 3D shape with a dynamically tunable structure enhances the applications of the fabricated imaging system, which can mimic the functionality of the biological eyes (*44*). The convex hemispherical structures of the Si-NM PD pixel arrays obtained in our gas pressure–induced bulging approach represent the compound eye structure of insects for wide-angle light detection. To demonstrate the wide field-of-view imaging ability of the evolved hemispherical structure, a narrow beam of 532-nm light was projected with the help of an optical fiber on both sides of the hemispherical PD matrix array, making an angle of ~20° on each side from the vertical axis at the center of the hemisphere. Figure 4D shows the photographic images of the measurement setup used for sensing the projected light at various incident directions and the corresponding mapping profiles produced in 3D format representing the convex surface of the PD array. It can be noticed from the acquired mapping images that the PD pixels directly facing the incident laser beam perpendicularly exhibit higher photoresponse, whereas the nearby pixels exhibit a slightly lower photocurrent. When the optical fiber-guided incident laser light moved to the other side of the hemispherical surface, a similar imaging trend was observed, where PD pixels at the other side of the matrix-faced incident light become responsive. These results conceptually reveal the benefits of the evolved convex 3D hemispherical layout of a Si-NM PD pixel matrix toward detecting and tracking light from wide incident angles in a manner similar to that in the case of the insect's eyes.

Apart from the convex hemispherical geometry, in our pneumatic pressure–induced bulging approach, the PD pixel arrays can also be realized in a reverse manner producing a concave structure. The PD pixels arranged in an inverted hemispherical geometry can mimic the concave focal plane of a mammalian's eye, where light is focused by a planoconvex lens (*2*, *44*). To realize the concave geometry, the Si-NM PD pixel array devices were mounted on the opposite surface of the PI film, and the photodetection characteristics were investigated by shining light through a glass window at the wall of the bulge test holder. With a gradual increase in the straining pressure, together with an increase in strain on the PD pixels, the curvature of the surface containing PD pixels also increased (Fig. 5, A and B). Similar to the convex case, the strain-driven imaging of the Y alphabet can be realized under the exposure of 1310-nm light with the prepared inverted structure at different straining pressures (Fig. 5A). The primary advantage of the gas pressure–induced formation of a concave structure is its dynamic tunability of surface curvature, which simultaneously aligns the PD pixels in a coordinated manner and provides a tunable zoom capability. To explore the benefits of the concave architecture in imaging, the collimated light beam was projected on the PD pixel array having different surface curvatures through a planoconvex lens. The image of an object formed by a planoconvex lens lies on a nonplanar hemispherical focal plane (Petzval surface), where a light beam on the planar screen is focused as a circular spot with decreasing intensity toward the center of the circle (*44*, *45*). Figure 5C shows the mapping image recorded with the PD arrays adhered onto the dynamically tunable concave surface. It can be noticed that the PD arrays under a flat condition (no applied straining pressure) exhibit a nonuniform photoresponse with higher photocurrent in the outer pixels. As the straining pressure increased, the

Downloaded from http://advances.sciencemag.org/ on December 4, 2020

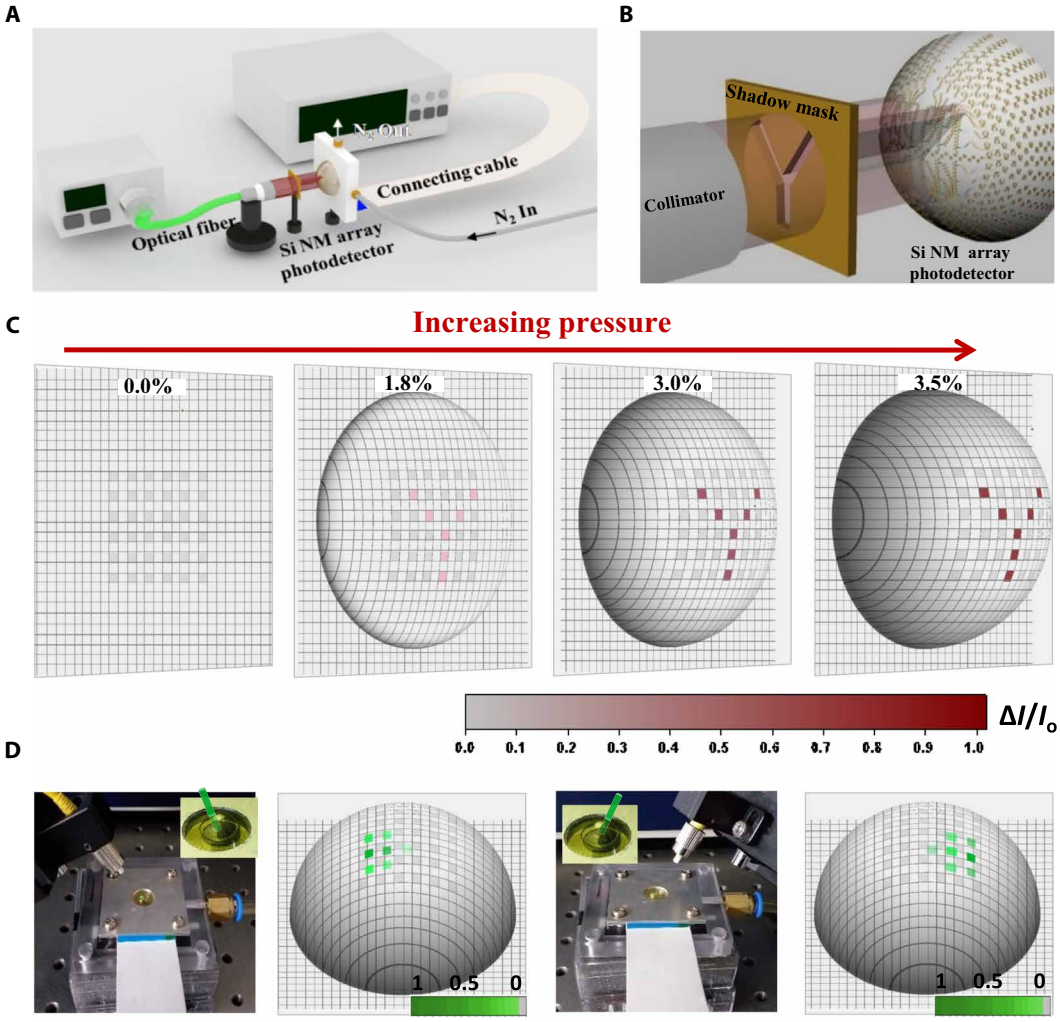

Fig. 4. Overview of optical imaging system and object images obtained from 6 × 6 Si-NM PD array under increasing strain. (**A**) Schematic illustration of the overall imaging system and optical setup used for imaging of the letter Y containing a collimated light source, shadow mask, and device array. (**B**) Enlarged view of the schematic representation for imaging of Y alphabet. (**C**) Photocurrent mapping images of a representative letter recorded under incident light of 1310 nm with increasing straining pressure. An increase in photocurrent with increase in applied pressure is evident, which is a consequence of the increased strain in each Si NM pixel. (**D**) Photographic images and corresponding acquired mapping images of the fabricated PD pixel arrays under convex hemispherical geometry. The laser is projected at an incident angle of ~20° from the normal at both sides of the PD arrays. Photo credit: Ajit K. Katiyar, Yonsei University.

photocurrent in the inner pixels tended to increase, and at a straining pressure of 1600 torr, the photoresponses of the PD pixels across the entire matrix turned out to be nearly equal. The deformation of the PD array into a concave shape, due to the straining pressure, geometrically aligns the PD pixels in the position of the image projected by the planoconvex lens (at the hemispherical focal plane), and thus, the entire field of view of an object comes into focus (movie S2). To verify the advantage of the concave surface on imaging more explicitly, we recorded the photocurrent pattern of the alphabet "I" with the PD matrix array under planar and concave architectures (Fig. 5, D and E). The image in the flat state reveals a higher photoresponse in the pixels located near the periphery of the field of view that are at the focus points, whereas the PD pixels near the center, which are not in focus, exhibit a lower photoresponse. The pneumatic deformation of the PD matrix surface into a concave shape moves the center pixels toward the focal position of the planoconvex lens, thereby providing a uniform and much clearer representative image of the I alphabet. The PD systems organized in a hemispherical architecture with convex or concave geometry can provide distinctive benefits over the conventional planar design in terms of broad-angle light harvesting and adjustable zoom, similar to those of the eyes of biological species. The observed strain-driven SWIR photosensing capability with tunable wavelength range up to 1550 nm from the pristine Si in this study could provide a promising approach for expanding the capabilities of IR image sensors in lidar systems used in self-driving vehicles or night vision surveillance cameras with state-of-the-art CMOS processing on a Si platform.

DISCUSSION

We investigated and demonstrated the enhancement in photoresponse and SWIR photosensing capabilities of Si subjected to biaxial tensile strains. To introduce strain, a perfect platform was provided by thin Si NMs that were mechanically stretched (biaxially) using a bulge

Downloaded from http://advances.sciencemag.org/ on December 4, 2020

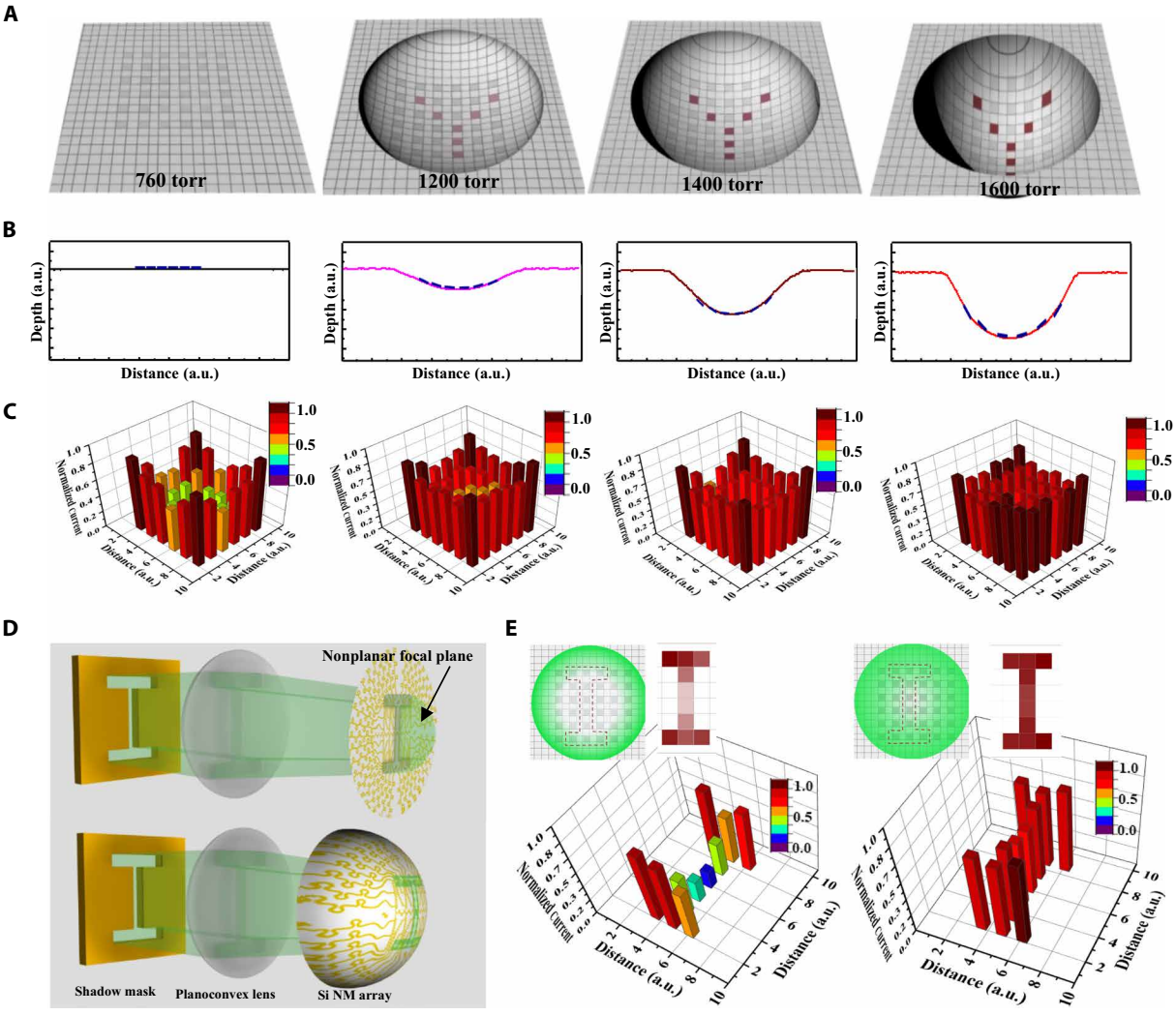

Fig. 5. Photoresponse obtained from 6 × 6 Si NM PD array under concave architecture. (**A**) Photocurrent mapping images of a representative letter recorded under incident light of 1310 nm with increasing straining pressure in concave geometry. (**B**) Curvature of concave surface PD pixel under increased straining pressure. (**C**) Photocurrent mapping image recorded with a light beam focused by a planoconvex lens onto the PD matrix system subjected to the increasing surface curvature. (**D**) Schematic representation of the photoresponse measurement of alphabet character I focused with planoconvex lens under flat and curved surface of PD matrix. (**E**) Representative mapping images of alphabet character I recorded with PD matrix under flat and concave architecture. Insets schematically show the light intensity distribution on the PD matrix surface under planar and curved geometry and corresponding photocurrent mapping image in 2D representation.

test setup. To explore the effect of strain on photosensing features, a simple MSM device was fabricated with a 10-nm-thick Si NM having a size of 20 μm by 20 μm on a stretchable PI substrate. The application of biaxial strain led to a substantial reduction in the optical bandgap of Si and allowed the detection of incident photons beyond the fundamental optical absorption limit of Si. This extension in the absorption limit of Si, in terms of photosensitivity, up to 1550 nm was observed with an applied biaxial strain of ~3.5%. Last, to demonstrate the imaging capability, a 6 × 6 matrix of an MSM PD array was fabricated, and the photocurrent pattern was recorded to map the representative images of an alphabet in SWIR light. The gas pressure–induced evolution of a hemispherical shape further extended the functionality of the fabricated PD arrays toward the mimicry of biological eyes, combining the simple origami approach with deformable optoelectronics. The results obtained in this study for the demonstration of SWIR sensing capability in Si with strain engineering could be very promising for many different applications that include Si-based IR image sensors and photovoltaics.

MATERIALS AND METHODS

Fabrication of Si NM PD arrays on elastomeric membranes

Individually addressable Si-NM MSM PD arrays were fabricated on moderate p-doped, 10-nm-thick single-crystalline Si (<100>, 0.025 ohm·cm) using PI as the elastomeric substrate and serpentine Cr/Au as stretchable metal electrodes. The process begins by reducing the thickness of the top silicon layer of the SOI wafer (SOI Tech, top Si, bottom oxide, and Si substrate thicknesses of 100, 200, and 525 μm, respectively) through a repeated oxidation and etching process that can precisely control the thickness of Si with 0.7-nm resolution. After reducing the Si NM thickness to 10 nm, a 6 × 6 array square matrix system of Si NMs as a photosensing pixel with a size

Downloaded from http://advances.sciencemag.org/ on December 4, 2020

of 20 μm by 20 μm and a distance of 280 μm between each pixel was created using conventional photolithography and the reactive ion etching process. The pixel size and separation were decided according to the applied maximum strain and required area for serpentine electrodes, respectively. The patterned array of Si NMs was released from the SOI wafer via wet etching in hydrofluoric acid (HF) for 25 min by dissolving buried oxide, and it was subsequently transfer-printed onto the semi-cured PI film (70°C for 1 hour) spin-coated on a SiO_2/Si substrate using a polydimethylsiloxane (PDMS) (SYLGARD 184 Silicone Elastomer Kit, Dow Corning) stamp. After attaching the PDMS stamp containing the Si NMs matrix, the entire assembly was baked at 105°C for 5 min to increase the adhesion between the Si and PI film. After releasing the PDMS stamp, the PI film on a SiO_2/Si substrate containing the array of Si NMs was fully cured at 300°C for 3 hours. To finalize the fabrication of the MSM device, the stretchable serpentine Cr/Au metal electrodes (2.5-nm Cr/ 25-nm Au) were deposited on each Si NM pixel using a combination of photolithography, thermal evaporation, and lift-off process.

Bulge test setup for straining Si NMs

To apply strain in the Si-NM PD pixels bonded on the PI film, the application of external mechanical stress using the bulge test setup was used. The bulge test sample holder primarily consisted of a gas inlet and outlet connected to manual leak valves to enable the controlled flow of N_2 gas, and an empty cavity. For applying strain into the Si NM pixels, the entire assembly of the fabricated MSM-PD arrays was formed freestanding by gently peeling off the PI film from the carrier SiO_2/Si wafer and thereafter mounted and sealed by a nitrile rubber O-ring on the cavity of the bulge test setup (fig. S1). Strain was applied on the Si-NM PD pixels by using external mechanical stress via the bulge test setup, which is schematically illustrated in fig. S2. Under a controlled flow of N_2, the pressure inside the sample holder cavity increased, which enabled the bulging in the PI membrane. As the pressure (i.e., strain) increased inside the bulge test chamber, the PI film gradually bulged upward and thereby imposed a biaxial strain in the Si-NM PD pixels in a highly controlled manner that were strongly bonded and located at the center of the top surface of the bulging PI sphere. The strain in the plane of the Si NM pixels was measured by coupling the bulge test setup with a Raman spectroscopy instrument, and the strain value in each pixel was calibrated corresponding to the pressure in the sample holder cavity.

Photoresponse measurement

To evaluate the strain-induced photosensing tunability of a single MSM-PD pixel, the collimated light beam of various wavelengths in the range of 405 to 1550 nm was guided and projected normally onto the plane of the Si NM PD pixel through an optical fiber, and the current-voltage characteristics were recorded under increasing biaxial strains in the PD pixels using a source meter unit (Keithley 4200 SCS parameter analyzer, Keithley Instruments Inc.). To measure photoresponse from the array device, the completed 6 × 6 matrix array device was connected to a ribbon cable for interfacing with an external data acquisition system (DAQ), where the individual PD unit was controlled sequentially by the applied bias. Under the exposure of the collimated light sources, the photoresponse of the array system was measured in real time by using a DAQ (Keithley 3706A) and a source meter (Keithley 2612) that recorded the photoresponses of the 36 devices with ~64-Hz intervals (corresponding to a frame interval of ~0.75 s). The raw photoresponse data obtained in the form of photocurrent from the DAQ were represented in a color intensity–coded scale for individual pixels to visualize the photocurrent mapping. As schematically shown in Fig. 4 (A and B), for the imaging of an alphabet character, an alphabet template was kept in between the light beam and the PD array subjected to increasing straining pressure, and the photoresponse of each pixel was recorded using the DAQ system. Under the influence of the shadow image, light was projected onto the PD array in a manner that maintained the original geometry of the alphabet; it only exposed particular pixels and switched them on, whereas other pixels under the opaque part of the shadow mask remained in the off state. By locating the pixel number corresponding to the position coordinates, the photocurrent pattern under the exposure of 1310-nm light was generated.

SUPPLEMENTARY MATERIALS

Supplementary material for this article is available at http://advances.sciencemag.org/cgi/content/full/6/31/eabb0576/DC1

REFERENCES AND NOTES

1. Y. M. Song, Y. Xie, V. Malyarchuk, J. Xiao, I. Jung, K. J. Choi, Z. Liu, H. Park, C. Lu, R. H. Kim, R. Li, K. B. Crozier, Y. Huang, J. A. Roger, Digital cameras with designs inspired by the arthropod eye. *Nature* **497**, 95–99 (2013).
2. I. Jung, J. Xiao, V. Malyarchuk, C. Lu, M. Li, Z. Liu, J. Yoon, Y. Huang, J. A. Rogers, Dynamically tunable hemispherical electronic eye camera system with adjustable zoom capability. *Proc. Natl. Acad. Sci. U.S.A.* **108**, 1788–1793 (2011).
3. X. Liu, B. Kuyken, G. Roelkens, R. Baets, R. M. Osgood Jr., W. M. J. Green, Bridging the mid-infrared-to-telecom gap with silicon nanophotonic spectral translation. *Nat. Photonics* **6**, 667–671 (2012).
4. A. Luque, A. Martí, Photovoltaics: Towards the intermediate band. *Nat. Photonics* **5**, 137–138 (2011).
5. Y. Kang, H. D. Liu, M. Morse, M. J. Paniccia, M. Zadka, S. Litski, G. Sarid, A. Pauchard, Y.-H. Kuo, H. W. Chen, W. S. Zaoui, J. E. Bowers, A. Beling, D. C. McIntosh, X. Zheng, J. C. Campbell, Monolithic germanium/silicon avalanche photodiodes with 340 GHz gain-bandwidth product. *Nat. Photonics* **3**, 59–63 (2008).
6. J. Michel, J. Liu, L. C. Kimerling, High-performance Ge-on-Si photodetectors. *Nat. Photonics* **4**, 527–534 (2010).
7. J. K. Doylend, P. E. Jessop, A. P. Knights, Silicon photonic resonator enhanced defect-mediated photodiode for sub-bandgap detection. *Opt. Express* **18**, 14671–14678 (2010).
8. M. W. Geis, S. J. Spector, M. E. Grein, R. T. Schulein, J. U. Yoon, D. M. Lennon, C. M. Wynn, S. T. Palmacci, F. Gan, F. X. Kärtner, T. M. Lyszczarz, All silicon infrared photodiodes: Photo response and effects of processing temperature. *Opt. Express* **15**, 16886–16895 (2007).
9. J. P. Mailoa, A. J. Akey, C. B. Simmons, D. Hutchinson, J. Mathews, J. T. Sullivan, D. Recht, M. T. Winkler, J. S. Williams, J. M. Warrender, P. D. Pearsans, M. J. Aziz, T. Buonassisi, Room-temperature sub-band gap optoelectronic response of hyperdoped silicon. *Nat. Commun.* **5**, 3011 (2014).
10. Y. Berencén, S. Prucnal, F. Liu, I. Skorupa, R. Hübner, L. Rebohle, S. Zhou, H. Schneider, M. Helm, W. Skorupa, Room-temperature short wavelength infrared Si photodetector. *Sci. Rep.* **7**, 43683 (2017).
11. K.-H. Hong, J. Kim, S.-H. Lee, J. K. Shin, Strain-driven electronic band structure modulation of Si nanowires. *Nano Lett.* **8**, 1335–1340 (2008).
12. S. Z. Karazhanov, A. Davletova, A. Ulyashin, Strain-induced modulation of band structure of silicon. *J. Appl. Phys.* **104**, 024501 (2008).
13. D. Shiri, Y. Kong, A. Buin, M. P. Anantram, Strain induced change of bandgap and effective mass in silicon nanowires. *Appl. Phys. Lett.* **93**, 073114 (2008).
14. D. Yu, Y. Zhang, F. Liu, First-principles study of electronic properties of biaxially strained silicon: Effects on charge carrier mobility. *Phys. Rev. B* **78**, 245204 (2008).
15. K. Yoshimoto, R. Suzuki, Y. Ishikawa, K. Wada, Bandgap control using strained beam structures for Si photonic devices. *Opt. Express* **18**, 26493–26498 (2010).
16. W. Lee, Y. Hwangbo, J.-H. Kim, J.-H. Ahn, Mobility enhancement of strained Si transistors by transfer printing on plastic substrates. *NPG Asia Mater.* **8**, e256 (2016).
17. K. Kusova, P. Hapala, J. Valenta, P. Jelinek, O. Cibulka, L. Ondic, I. Pelant, Direct bandgap silicon: Tensile-strained silicon nanocrystals. *Adv. Mater. Interfaces* **1**, 1300042 (2014).
18. J. Munguia, G. Bremond, J. M. Bluet, J. M. Hartmann, M. Mermoux, Strain dependence of indirect band gap for strained silicon on insulator wafers. *Appl. Phys. Lett.* **93**, 102101 (2008).
19. M. H. Liao, T. H. Cheng, C. W. Liu, Infrared emission from Ge metal-insulator-semiconductor tunneling diodes. *Appl. Phys. Lett.* **89**, 261913 (2006).

Downloaded from http://advances.sciencemag.org/ on December 4, 2020

20. Y. Sun, S. E. Thompson, T. Nishida, Physics of strain effects in semiconductors and metal-oxide-semiconductor field-effect transistors. *J. Appl. Phys.* **101**, 104503 (2007).
21. A. R. Adams, Band structure engineering for low threshold high efficiency semiconductor lasers. *Electron. Lett.* **22**, 249–250 (1986).
22. G. C. Osbourn, $In_xGa_{1-x}As$-$In_yGa_{1-y}As$ strained-layer superlattices: A proposal for useful, new electronic materials. *Phys. Rev. B* **27**, 5126–5128 (1983).
23. M. Cazzanelli, F. Bianco, E. Borga, G. Pucker, M. Ghulinyan, E. Degoli, E. Luppi, V. Veniard, S. Ossicini, D. Modotto, S. Wabnitz, R. Pierobon, L. Pavesi, Second-harmonic generation in silicon waveguides strained by silicon nitride. *Nat. Mater.* **11**, 148–154 (2012).
24. M. Takenaka, S. Takagi, Strain engineering of plasma dispersion effect for SiGe optical modulators. *IEEE J. Quantum Electron.* **48**, 8–16 (2012).
25. J. D. Cressler, *SiGe and Si Strained-Layer Epitaxy for silicon heterostructure devices* (CRC Press, Taylor and Francis Group, 2017).
26. J. Cai, Y. Ishikawa, K. Wada, Strain induced bandgap and refractive index variation of silicon. *Opt. Express* **21**, 7162–7170 (2013).
27. R. He, P. Yang, Giant piezoresistance effect in silicon nanowires. *Nat. Nanotechnol.* **1**, 42–46 (2006).
28. H. Zhang, J. Tersoff, S. Xu, H. Chen, Q. Zhang, K. Zhang, Y. Yang, C. S. Lee, K. N. Tu, J. Li, Y. Lu, Approaching the ideal elastic strain limit in silicon nanowires. *Sci. Adv.* **2**, e1501382 (2016).
29. Z. Mu, M. Zhang, Z. Xue, G. Sun, Q. Guo, D. Chen, G. Huang, Y. Mei, P. K. Chu, Z. Di, X. Wang, Manipulation of strain state in silicon nanoribbons by top-down approach. *Appl. Phys. Lett.* **106**, 174102 (2015).
30. See supplementary materials on Science Online.
31. M. J. Buehler, H. Tang, A. C. Duin, W. A. Goddard, Threshold crack speed controls dynamical fracture of silicon single crystals. *Phys. Rev. Lett.* **99**, 165502 (2007).
32. G. Kresse, J. Furthmüller, Efficient iterative schemes for ab initio total-energy calculations using a plane-wave basis set. *Phys. Rev. B* **54**, 11169–11186 (1996).
33. P. E. Blochl, Projector augmented-wave method. *Phys. Rev. B* **50**, 17953–17979 (1994).
34. J. P. Perdew, K. Burke, M. Ernzerhof, Generalized gradient approximation made simple. *Phys. Rev. Lett.* **77**, 3865–3868 (1996).
35. P. Zhang, E. Tevaarwerk, B. N. Park, D. E. Savage, G. K. Celler, I. Knezevic, P. G. Evans, M. A. Eriksson, M. G. Lagally, Electronic transport in nanometre-scale silicon-on-insulator membranes. *Nature* **439**, 703–706 (2006).
36. L.-P. Boivin, Spectral responsivity of various types of silicon photodiode at oblique incidence: Comparison of measured and calculated values. *Appl. Optics* **40**, 485–491 (2001).
37. C. Battaglia, A. Cuevas, S. D. Wolf, High-efficiency crystalline silicon solar cells: Status and perspectives. *Energ. Environ. Sci.* **9**, 1552–1576 (2016).
38. M. S. Kim, G. J. Lee, H. M. Kim, Y. M. Song, Parametric optimization of lateral NIPIN phototransistors for flexible image sensors. *Sensors* **17**, 1774 (2017).
39. H. Li, A. W. Contryman, X. Qian, S. M. Ardakani, Y. Gong, X. Wang, J. M. Weisse, C. H. Lee, J. Zhao, P. M. Ajayan, J. Li, H. C. Manoharan, X. Zheng, Optoelectronic crystal of artificial atoms in strain-textured molybdenum disulphide. *Nat. Commun.* **6**, 7381 (2015).
40. V. S. Mangu, M. Zamiri, S. R. J. Brueck, F. Cavallo, Strain engineering, efficient excitonic photoluminescence, and exciton funnelling in unmodified MoS_2 nanosheets. *Nanoscale* **9**, 16602–16606 (2017).
41. Y. Yu, Y. Zhang, X. Song, H. Zhang, M. Cao, Y. Che, H. Dai, J. Yang, H. Zhang, J. Yao, PbS-decorated WS_2 phototransistors with fast response. *ACS Photonics* **4**, 950–956 (2017).
42. C. Liu, M. L. Lovato, K. D. Clarke, D. J. Alexander, W. R. Blumenthal, Miniature bulge test and energy release rate in HIPed aluminum/aluminum interfacial fracture. *J. Mech. Phys. Solids* **120**, 179–198 (2018).
43. Z. X. Hou, E. R. Liu, A. Feng, Z. R. Wang, Finite element analysis of hemispherical-shape parts in the hot gas bulge-forming of polycarbonate (PC) sheet. *Appl. Mech. Mater.* **10–12**, 140–144 (2008).
44. H. C. Ko, M. P. Stoykovich, J. Song, V. Malyarchuk, W. M. Choi, C. J. Yu, J. B. Geddes III, J. Xiao, S. Wang, Y. Huang, J. A. Rogers, A hemispherical electronic eye camera based on compressible silicon optoelectronics. *Nature* **454**, 748–753 (2008).
45. K. Zhang, Y. H. Jung, S. Mikael, J.-H. Seo, M. Kim, H. Mi, H. Zhou, Z. Xia, W. Zhou, S. Gong, Z. Ma, Origami silicon optoelectronics for hemispherical electronic eye systems. *Nat. Commun.* **8**, 1782 (2017).

Acknowledgments

Funding: This work was supported by the National Research Foundation of Korea (NRF) funded by the Korean government (MSIT) (NRF-2015R1A3A2066337). **Author contributions:** J.-H.A. planned and supervised the project. A.K.K. conducted most of the experiments regarding the device fabrication and characterized the optoelectronic properties of the devices. A.K.K., J.L., and J.-H.A. wrote the manuscript. K.Y.T. fabricated the array devices. W.S.Y. and J.L. conducted the theoretical calculations. **Competing interests:** The authors declare that they have no competing interests. **Data and materials availability:** All data needed to evaluate the conclusions in the paper are present in the paper and/or the Supplementary Materials. Additional data related to this paper may be requested from the authors.

Submitted 27 January 2020
Accepted 9 June 2020
Published 29 July 2020
10.1126/sciadv.abb0576

Citation: A. K. Katiyar, K. Y. Thai, W. S. Yun, J. Lee, J.-H. Ahn, Breaking the absorption limit of Si toward SWIR wavelength range via strain engineering. *Sci. Adv.* **6**, eabb0576 (2020).

Downloaded from http://advances.sciencemag.org/ on December 4, 2020

Science Advances

Breaking the absorption limit of Si toward SWIR wavelength range via strain engineering

Ajit K. Katiyar, Kean You Thai, Won Seok Yun, JaeDong Lee and Jong-Hyun Ahn

Sci Adv **6** (31), eabb0576.
DOI: 10.1126/sciadv.abb0576

ARTICLE TOOLS http://advances.sciencemag.org/content/6/31/eabb0576

SUPPLEMENTARY MATERIALS http://advances.sciencemag.org/content/suppl/2020/07/27/6.31.eabb0576.DC1

REFERENCES This article cites 43 articles, 2 of which you can access for free
http://advances.sciencemag.org/content/6/31/eabb0576#BIBL

PERMISSIONS http://www.sciencemag.org/help/reprints-and-permissions

Use of this article is subject to the Terms of Service

Science Advances (ISSN 2375-2548) is published by the American Association for the Advancement of Science, 1200 New York Avenue NW, Washington, DC 20005. The title *Science Advances* is a registered trademark of AAAS.

Copyright © 2020 The Authors, some rights reserved; exclusive licensee American Association for the Advancement of Science. No claim to original U.S. Government Works. Distributed under a Creative Commons Attribution NonCommercial License 4.0 (CC BY-NC).

Downloaded from http://advances.sciencemag.org/ on December 4, 2020